

Spatial frequency domain correlation mapping optical coherence tomography for nanoscale structural characterization

Cite as: Appl. Phys. Lett. **115**, 121105 (2019); <https://doi.org/10.1063/1.5110459>

Submitted: 11 June 2019 . Accepted: 03 September 2019 . Published Online: 16 September 2019

Sergey Alexandrov , Paul M. McNamara , Nandan Das , Yi Zhou , Gillian Lynch, Josh Hogan, and Martin Leahy 



View Online



Export Citation



CrossMark

ARTICLES YOU MAY BE INTERESTED IN

[Optical synthetic sampling imaging: Concept and an example of microscopy](#)

Applied Physics Letters **115**, 121101 (2019); <https://doi.org/10.1063/1.5115448>

[Picosecond nonlinear spintronic dynamics investigated by terahertz emission spectroscopy](#)

Applied Physics Letters **115**, 121104 (2019); <https://doi.org/10.1063/1.5117179>

[Ambipolar transistor action of germanane electric double layer transistor](#)

Applied Physics Letters **115**, 122101 (2019); <https://doi.org/10.1063/1.5094817>

Lock-in Amplifiers up to 600 MHz

starting at

\$6,210



 Zurich Instruments

Watch the Video 

AIP
Publishing

Spatial frequency domain correlation mapping optical coherence tomography for nanoscale structural characterization

Cite as: Appl. Phys. Lett. **115**, 121105 (2019); doi: [10.1063/1.5110459](https://doi.org/10.1063/1.5110459)

Submitted: 11 June 2019 · Accepted: 3 September 2019 ·

Published Online: 16 September 2019



View Online



Export Citation



CrossMark

Sergey Alexandrov,^{1,a)}  Paul M. McNamara,²  Nandan Das,¹  Yi Zhou,¹  Gillian Lynch,¹ Josh Hogan,³ and Martin Leahy¹ 

AFFILIATIONS

¹National University of Ireland, Tissue Optics and Microcirculation Imaging Facility, School of Physics, National Biophotonics and Imaging Platform, Galway H91 CF50, Ireland

²Compact Imaging Ireland, Ltd., Roselawn House, National Technology Park, Limerick V94 6R68, Ireland

³Compact Imaging, Inc., 897 Independence Ave., Suite 5B, Mountain View, California 94043, USA

^{a)} Author to whom correspondence should be addressed: sergey.alexandrov@nuigalway.ie

ABSTRACT

Most of the fundamental pathological processes in living tissues exhibit changes at the nanoscale. Noninvasive, label-free detection of structural changes in biological samples pose a significant challenge to both researchers and healthcare professionals. It is highly desirable to be able to resolve these structural changes, during physiological processes, both spatially and temporally. Modern nanoscopy largely requires labeling, is limited to superficial 2D imaging, and is generally not suitable for *in vivo* applications. Furthermore, it is becoming increasingly evident that 2D biology often does not translate into the real 3D situation. Here, we present a method, spatial frequency domain correlation mapping optical coherence tomography (sf-cmOCT), for detection of depth resolved nanoscale structural changes noninvasively. Our approach is based on detection and correlation of the depth resolved spectra of axial spatial frequencies of the object which are extremely sensitive to structural alterations. The presented work describes the principles of this approach and demonstrates its feasibility by monitoring internal structural changes within objects, including human skin *in vivo*. Structural changes can be visualized at each point in the sample in space from a single image or over time using two or more images. These experimental results demonstrate possibilities for the study of nanoscale structural changes, without the need for biomarkers or labels. Thus, sf-cmOCT offers exciting and far-reaching opportunities for early disease diagnosis and treatment response monitoring, as well as a myriad of applications for researchers.

© 2019 Author(s). All article content, except where otherwise noted, is licensed under a Creative Commons Attribution (CC BY) license (<http://creativecommons.org/licenses/by/4.0/>). <https://doi.org/10.1063/1.5110459>

Various pathologies, such as atherosclerosis, cancers, small tumors, and liver cirrhosis, lead to changes in the structure of the affected tissues. At the early onset of a disease, these changes manifest themselves at a cellular level (submicron scale). The existing clinical gold standards, magnetic resonance imaging^{1,2} and ultrasound,^{3,4} are only sensitive to large scale changes (0.1–1 mm). Recently, the diffraction resolution limit has been broken and optical nanoscale microscopy has been developed.^{5–8} But modern nanoscopy largely requires labeling, is limited to superficial 2D imaging, and is not suitable for *in vivo* applications.

Optical coherence tomography (OCT),⁹ the optical analog of ultrasound imaging, has started to revolutionize medical diagnostics. Various modalities of OCT have been developed and adapted for

different problems.^{10–13} Numerous OCT-based angiography (OCTA) techniques have been proposed,^{14,15} including speckle-variance (SV) and Doppler OCT, both of which have been commercialized. The correlation mapping OCT (cmOCT) technique was proposed to map microvasculature networks noninvasively *in vivo*,^{16–18} and its extension, cube cmOCT, has been published.¹⁹ But resolution and sensitivity to structural alterations of conventional OCT intensity based imaging are limited.

The coherent transfer function of the OCT is centered at zero lateral spatial frequencies but shifted to high axial spatial frequencies, larger than 1000 1/mm.²⁰ So the OCT signal is formed by light scattered from the small, submicrometer structure and is ultrasensitive to structural changes. However, during the reconstruction process via

Fourier transform, information about high spatial frequencies (small structure) is lost. In fact, the result of the Fourier transform does not depend on the location of the Fourier spectrum. So if the OCT signal is formed by scattering on small, submicron structures or is formed by scattering on large, micrometer scale structures, the result will be the same as it depends on the spatial frequency bandwidth only. The depth resolution of OCT in terms of spatial frequency can be written as

$$R_z \approx \frac{4\ln 2}{n\pi\Delta\nu_z}, \quad (1)$$

where $\Delta\nu_z$ is the bandwidth of the accessible spatial frequencies of the object which depends on the spectral bandwidth of the illumination. From (1), we can see that the resolution depends on the bandwidth of spatial frequency $\Delta\nu_z$ only and does not depend on the location of this bandwidth in the Fourier domain.

A label-free spectral encoding of spatial frequency (SESF) approach for visualization of nanoscale structural alterations has previously been developed^{21–24} and applied for super-resolution imaging.^{24,25} It was demonstrated that spatial frequency components of the 3D Fourier spectrum of the object can be spectrally encoded as corresponding wavelengths and passed through the imaging system independent of the resolution.^{21–26} But only 2D implementation of this approach has been published.

The nsOCT method was invented to retain the high spatial frequency information in OCT imaging. The technique permits depth resolved visualization of the dominant size of the structure with nanoscale sensitivity.^{27–29} Recently, the nsOCT has been successfully applied to detect nanometer scale structural changes in the tympanic membrane.³⁰

In this letter, we propose a different technique, spatial frequency domain correlation mapping OCT (sf-cmOCT) which permits depth resolved detection and visualization of the nanoscale structural changes. Feasibility and advantages of this approach are demonstrated in different realizations to detect structural changes in space and in time, by imaging various objects including human skin *in vivo*.

sf-cmOCT works by reconstructing and correlating the axial spatial frequency profile (ASFP) or period (ASPP) available for each pixel of the nsOCT image. The correlation can be done between ASFPs at a given point and profiles at all other points or between ASFP of one image and corresponding profiles of other images, for example, recorded at a different moment in time, and so on. The presented version of the sf-cmOCT is based on the Pearson correlation formula used in cmOCT,^{16–18,31} but with fundamental differences. Rather than calculating the contrast between intensities within intensity based images, sf-cmOCT reveals differences in the spatial frequency content, and so structural changes at a given location in time or between spatial locations are detected. Areas of similar spatial frequency content, or similar structure, will have high correlation, whereas areas with differing structures (differing spatial frequency content) will have low correlation. The result is a correlation map based on the structural information. This approach, in contrast to cmOCT, permits improvement of sensitivity up to the nanoscale and the visualization of structural changes both in space and in time.

As a proof of concept experiment, sf-cmOCT was used to image two samples from OptiGrate Corp. USA, with different axial periodic structures, where the corresponding periods are 431.6 and 441.7 nm

(Fig. 1). To demonstrate the potential abilities of the sf-cmOCT to detect even smaller structural changes, we performed a numerical simulation of this imaging and added an additional area with a period of 428.6 nm. The OCT signal was formed as interference of the reflected light with the reference wave. The randomized noise spectra were added to mimic experimental reality, signal to noise ratio (SNR) = 76 dB. The inverse Fourier transform was used to form a B-scan of these samples, presented in Fig. 1(a).

An experimental spectral domain OCT (SDOCT) image of this sample, obtained using a TELESTO III from Thorlabs, Inc., is presented in Fig. 1(c). The sf-cmOCT images in Figs. 1(b) and 1(d) were formed as color maps of correlation between ASFP at one point within the area with a 431.6 nm period of structure and ASFPs at all other points within the image. Hence, all areas with a similar structure are visualized with the same color according to the color bar. We also imaged an infrared card (VRC2 from Thorlabs, Inc.) for comparison. The depth of the preliminary sf-cmOCT image was reduced by thresholding, but further optimization could increase it.

In conventional OCT images in Figs. 1(a) and 1(c), it is impossible to detect areas with different structures, but in the sf-cmOCT images in Figs. 1(b) and 1(d), which are based on a different contrast mechanism, all areas with different structures can be clearly distinguished as different colors, including the antireflection coating on the top of the samples, as seen in Fig. 1(d). In the simulated image in Fig. 1(b), differences in the dominant size of the structure as small as 3 nm can be clearly detected as areas with red and orange colors. The infrared card has a complicated structure, which visualizes as different correlation coefficients at different locations within the card, and so different colors are present in the image at different locations. Both numerical simulations and experimental results confirmed sensitivity to structural changes of about 10 nm.

For other experiments, a custom-built SDOCT was used. A broadband superluminescent diode (DenseLight, Singapore) centered on 1310 nm provided an axial resolution of approximately 10 μm in

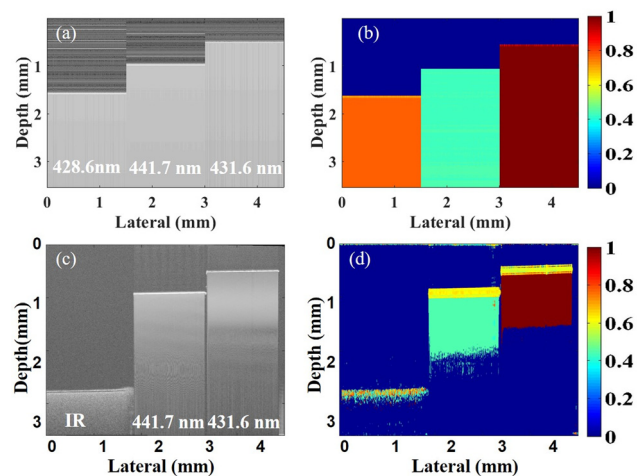


FIG. 1. Numerically simulated (a) and (b) and experimental (c) and (d) conventional OCT (a) and (c) and sf-cmOCT (b) and (d) images of the samples consisting of areas with periodic structures with different spatial periods. The image of the infrared card is presented on the left in experimental images for comparison. The color bar presents the correlation coefficients.

air. The lateral resolution was approximately $14\ \mu\text{m}$ in air. The recombined light from both arms was passed to a high-resolution spectrometer (BaySpec, NJ, USA) providing an imaging depth of 3.5 mm.

The next experiment demonstrates the ability of the sf-cmOCT to visualize structural changes in space. A glass tube filled with milk was embedded in BluTack (Bostik Industries) and used as the sample. The SDOCT system used to collect the data was inherently noisy, and hence, the signal to noise ratio (SNR) between the signal area (yellow) and the noise area (red) in Fig. 2(a) in the SDOCT image was about 31 dB. The tube with milk is orientated perpendicular to the cross-sectional images (B-scans) shown in Fig. 2. Both SDOCT (intensity) and sf-cmOCT images were formed using a single frame. In the SDOCT B-scan, the structures within the tube with milk and the outside of tube appear similar. The ASPPs have been reconstructed for each location within the image. In Fig. 2(a), the examples of two such profiles, reconstructed at single pixel within the area outside of the tube with milk (within the yellow rectangle) and at a pixel within the tube with milk, are presented. These profiles provide information about the structural sizes within the collected range of spatial frequencies. The profiles are different, implying that the corresponding structures within the tube and outside the tube are different. Based on this difference, in the sf-cmOCT image, formed as a correlation between ASFP within BluTack and ASFPs at all other points, the areas with different structures (within the tube and out of tube) are clearly visualized using just one frame.

To demonstrate the ability of the sf-cmOCT to visualize structural changes in time, we imaged Brownian motion within the tube of milk, Fig. 3. In this case, the sf-cmOCT image, Fig. 3(b), is generated as a correlation map where the correlation is calculated between the ASFPs within the image, recorded at one moment in time, and corresponding profiles within the image, recorded 20 ms later. The sf-cmOCT permits the static and dynamic areas within the sample to be clearly distinguished, allowing visualization of both in Fig. 3(b).

For visualization of structural changes in time, the OCTA techniques can be used. It was known that OCTA techniques, especially phase based OCTA, do not work well at a high level of noise^{14,15} and

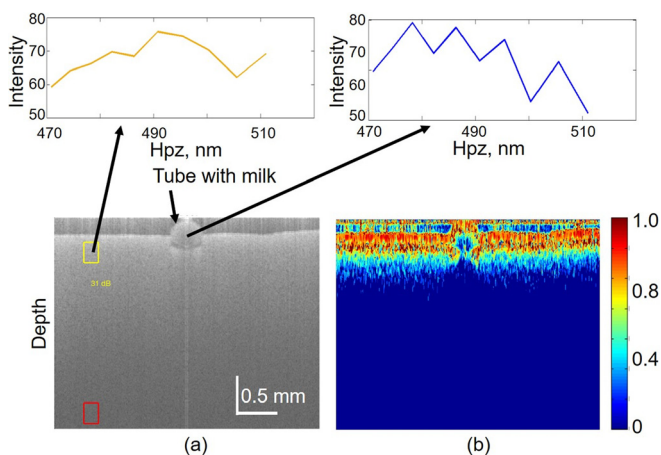


FIG. 2. (a)—Conventional SDOCT intensity image and (b)—sf-cmOCT images of tube with milk. Axial spatial period profiles (ASFPs) reconstructed at some location within the BluTack (within the yellow rectangle) and at some location within the tube of milk, also shown.

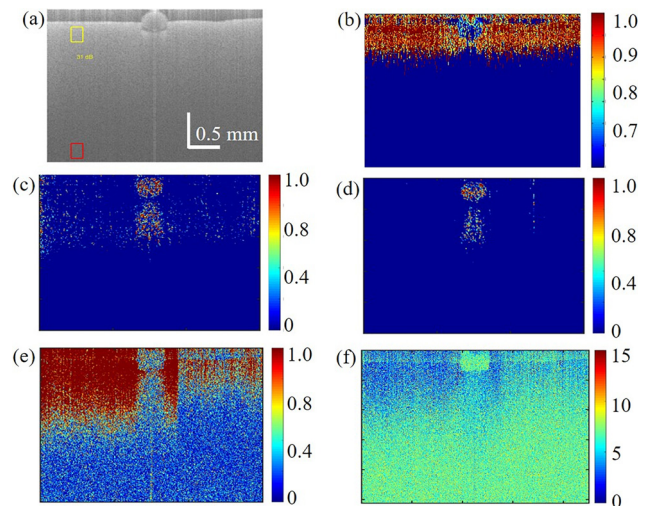


FIG. 3. Depth resolved imaging of a glass tube containing milk, (a) conventional SDOCT image, (b) sf-cmOCT image formed using two frames, (c) cmOCT image, (d) cube cmOCT image, (e) speckle variance (SV) image, and (f) phase variance image. The scale bar is 0.5 mm in each direction.

would be interesting to see images, based on the same noisy data, formed using different OCTA techniques. The corresponding images are presented in Figs. 3(c)–3(f). The cmOCT image, shown in Fig. 3(c), was formed using two consecutive frames. The cube cmOCT image in Fig. 3(d) was formed using 5 consecutive frames. This image has better contrast and less noise than the cmOCT image (due to the statistical effect of using more voxels) but contains similar artifacts. To form the speckle variance (SV) image in Fig. 3(e), 7 frames were used. To form the phase variance (PV) image in Fig. 3(f), 20 frames were used. Figures 3(c)–3(f) show that all these known techniques do not work well on such noisy data. For example, the flow area in these images can also be detected below the tube with milk, in the static BluTack region, where there is no flow. The location of the static areas is also not clear in this instance. Only the sf-cmOCT technique demonstrates clear visualization of the static (BluTack) and dynamic (milk) regions.

In the next experiments, we applied the sf-cmOCT to different objects using the same SDOCT system. Images were acquired to analyze the structure within the *in vivo* nail fold of the human finger, before and during a simple occlusion test. A brachial arterial occlusion was applied using a sphygmomanometer on the upper left arm of the subject. A pressure of 200 mm-Hg was applied for a duration of 30 s. It was expected that such a pressure would reduce the blood flow in the capillaries of the nail fold, and hence, the corresponding tiny structural changes within the finger could be detected using sf-cmOCT. The sf-cmOCT images before and during the occlusion are presented in Figs. 4(a) and 4(b). Each of these images was generated using two consecutive frames separated by 20 ms. The ASFPs change during the time period between the two frames in Fig. 4(a) before occlusion but remain almost the same during occlusion in Fig. 4(b).

From comparison of Figs. 4(a) and 4(b), the correlation coefficient in Fig. 4(b) is higher in most areas than in Fig. 4(a) and is more uniform. This means that structural variations in time within the finger under occlusion are smaller and the structure is more stable

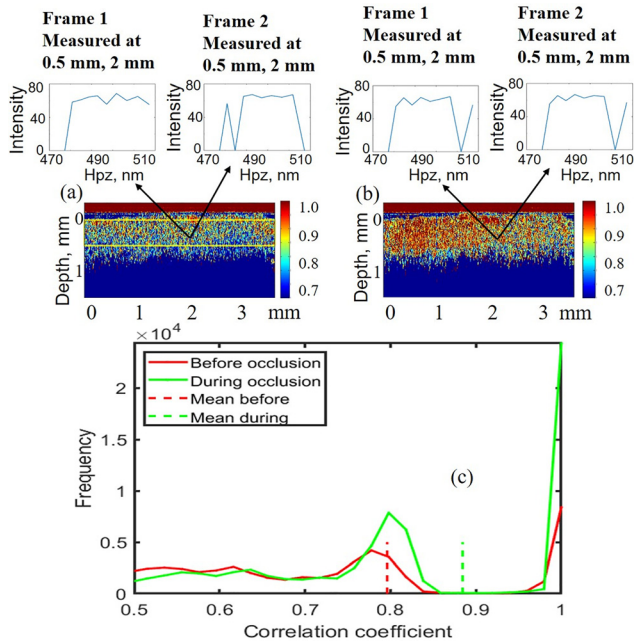


FIG. 4. sf-cmOCT images of the human finger *in vivo*: (a) before and (b) during occlusion, with examples of the axial spatial frequency profiles between consecutive frames. (c) Frequency distribution of correlation coefficients within the yellow region of interest before (red) and during (green) occlusion with the corresponding mean values.

than before the occlusion. Such tiny structural changes, calculated within an area of interest [denoted by the yellow rectangle in Fig. 4(a)], are shown in Fig. 4(c), where the corresponding frequency for correlation coefficient 1 is about 3 times larger than that before the occlusion and the mean correlation coefficients before and under occlusion are 0.796 and 0.885, respectively. This result suggests that small structural changes within the nail fold before

and under occlusion can be clearly detected and visualized using sf-cmOCT.

In the next experiment, we demonstrate the ability of the cm-nsOCT to visualize dynamics of the structural changes and show how fast these changes occur. The sample chosen was a light-activated dental resin composite (Gradia Direct Dental Hybrid Composite, GC America, Inc., USA). Light-activated resin composites are commonly used in restorative dental procedures³² and are composed of sub-micron particles. During curing, the absorption of light by photoinitiators begins a polymerization process,³³ inducing rapid structural changes. Free radicals are generated on the polymer chains and bond with one another to form a solidified 3D polymer network.³⁴ In this experiment, a small amount of resin ($3 \times 3 \times 1 \text{ mm}^3$) was applied to the surface of a glass coverslip and placed on a fixed stage in the sample arm. A blue LED source (M470L2, Thorlabs, USA) centered at 470 nm, with a measured irradiance of 800 mW/cm^2 at the sample surface, was used to activate the curing process.

A series of 2D OCT datasets were recorded in B-M mode for a total of 2 min for 3 different samples of the resin composite. B-M mode scanning refers to the repeated recording of a B-frame at one location over time. The sf-cmOCT plots for each dataset were generated by correlating the first B-frame (at $t = 0 \text{ s}$) with each subsequent B-frame, at time intervals Δt . To distinguish how quickly the structure is changing, the frequency content of the correlation signal was analyzed, color-coded, and mapped as a 2D image.

Figure 5 shows examples of images of the resin composite generated using conventional OCT as well as sf-cmOCT. As can be seen, the sf-cmOCT images acquired before and after curing [Figs. 5(d) and 5(f)] do not show a large amount of changes vs time dependences. However, in contrast to conventional OCT, during the curing process [Fig. 5(e)], the distinct change in the structure can be observed. Conventional OCT intensity images in Figs. 5(a)–5(c) and cmOCT³⁵ were unable to discern the structural changes occurring during the curing process. Our experiments show that while it is curing, the structure of the resin is undergoing dramatic structural changes, and consequently, the correlation coefficient between B-frames changes rapidly. However, before and

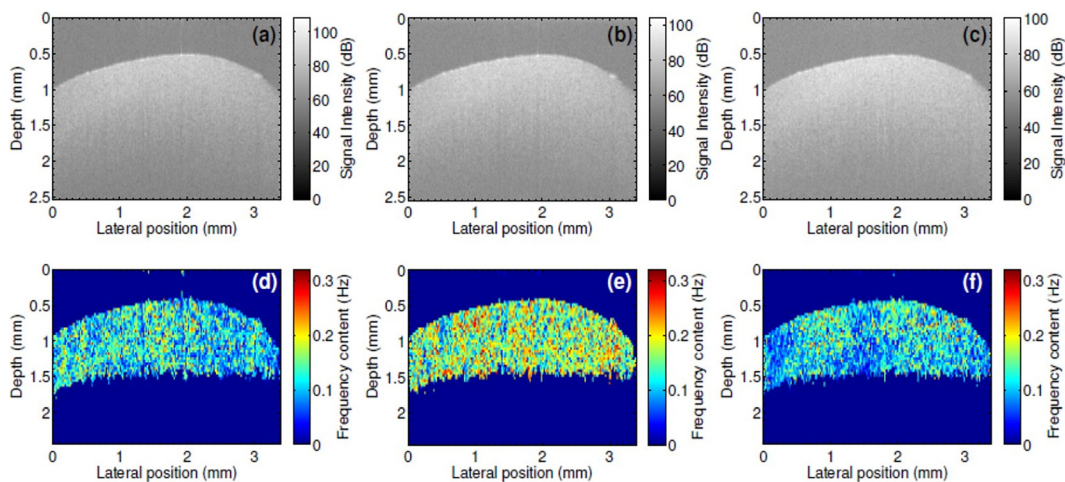


FIG. 5. OCT images acquired before (a), during (b), and after (c) curing; sf-cmOCT visualizations depicting structural changes occurring over a 10-s interval for before (d), during (e), and after (f) curing.

after curing, the sf-cmOCT does not show any rapid structural changes since the structure of the resin does not change at either of these times.

The presented label-free sf-cmOCT method is significantly different from both intensity based and phase sensitive OCT techniques for structural characterization. We have validated sf-cmOCT by showing that it can visualize areas with different structures in space from just a single frame (within the sample with a periodic structure with a sensitivity of about 10 nm and within milk) and structural changes in time (Brownian motion) within milk, detect structural changes *in vivo* within the nail fold of the human finger occurring under forearm occlusion, and detect how fast the structural changes occur due to polymer curing. The results of the numerical simulation suggest potential sensitivity to structural changes of down to 3 nm at an SNR = 76 dB. As shown by our results, the proposed approach dramatically extends the abilities of OCT to be sensitive to nanoscale structural alterations in space and in time. In addition, the lateral spatial resolution can be improved by adapting the methodology described in Refs. 25 and 26.

This project received funding from the European Union's Horizon 2020 research and innovation program under Grant Agreement Nos. 761214 and 779960. The materials presented and views expressed here are the responsibility of the author(s) only. The EU Commission takes no responsibility for any use made of the information set out.

Also, this work was supported by NUI Galway, Galway University Foundation, the University of Limerick Foundation, the National Biophotonics Imaging Platform (NBIP) Ireland funded under the Higher Education Authority PRTL Cycle 4 and co-funded by the Irish Government and the European Union, Compact Imaging, Inc., and Nandan Das received Government of Ireland postdoctoral fellowship grant with project ID: GOIPD/2017/837.

Sergey Alexandrov, Paul M. McNamara, Josh Hogan, and Martin Leahy have a financial interest in Compact Imaging, Inc. The authors have no other relevant financial interest in this article and no other potential conflicts of interest to disclose.

The acquisition of the *in-vivo* samples does not affect any ethical, health, or privacy concerns and was performed according to the ethical regulations and safety standards of the NUI Galway.

REFERENCES

- ¹S. A. Ara, G. Katti, and A. Shireen, *Int. J. Dent. Clinics* **3**(1), 65–70 (2011).
- ²Y. K. Mariappan, K. J. Glaser, and R. L. Ehman, *Clin. Anat.* **23**(5), 497–511 (2010).
- ³D. J. Martin, I. T. P. Wells, and C. R. Goodwin, *Anaesth. Intensive Care* **16**(3), 132–135 (2015).
- ⁴A. Tang, G. Cloutier, N. M. Szeverenyi, and C. B. Sirlin, *Am. J. Roentgenol.* **205**(1), 22–32 (2015).
- ⁵M. A. Lauterbach, *Opt. Nanosc.* **1**, 8 (2012).
- ⁶S. W. Hell, *Nat. Biotechnol.* **21**(11), 1347–1355 (2003).
- ⁷B. Huang, M. Bates, and X. W. Zhuang, *Annu. Rev. Biochem.* **78**, 993–1016 (2009).
- ⁸A. Barsic, G. Grover, and R. Piestun, *Sci. Rep.* **4**, 5388 (2014).
- ⁹D. Huang, E. A. Swanson, C. P. Lin, J. S. Schuman, W. G. Stinson, W. Chang, M. R. Hee, T. Flotte, K. Gregory, C. A. Puliafito, and J. G. Fujimoto, *Science* **254**(5035), 1178–1181 (1991).
- ¹⁰V. Y. Zaitsev, L. A. Matveev, A. L. Matveyev, G. V. Gelikonov, and V. M. Gelikonov, *Laser Phys. Lett.* **11**, 105601 (2014).
- ¹¹F. E. Robles, C. Wilson, G. Grant, and A. Wax, *Nat. Photonics* **5**(12), 744–747 (2011).
- ¹²T. S. Balston, D. L. Marks, P. S. Carney, and S. A. Boppart, *Nat. Phys.* **3**(2), 129–134 (2007).
- ¹³L. Cherkazyan, D. Zhang, H. Subramanian, I. Capoglu, A. Taflove, and V. Backman, *J. Biomed. Opt.* **22**(3), 030901 (2017).
- ¹⁴C. L. Chen and R. K. Wang, *Biomed. Opt. Express* **8**(2), 1056–1082 (2017).
- ¹⁵E. Borrelli, S. R. Sada, A. Uji, and G. Querques, *Ophthalmol. Ther.* **8**, 215–226 (2019).
- ¹⁶J. Enfield, J. McGrath, S. M. Daly, and M. Leahy, *J. Biomed. Opt.* **21**(8), 081212 (2016).
- ¹⁷E. Jonathan, J. Enfield, and M. J. Leahy, *J. Biophotonics* **4**(9), 583–587 (2011).
- ¹⁸P. M. McNamara, H. M. Subhash, and M. J. Leahy, *J. Biomed. Opt.* **18**(12), 126008 (2013).
- ¹⁹C. L. Chen, J. L. Liao, and W. R. Gao, *Opt. Eng.* **54**(4), 043104 (2015).
- ²⁰C. J. R. Sheppard, M. Roy, and M. D. Sharma, *Appl. Opt.* **43**(7), 1493–1502 (2004).
- ²¹S. Alexandrov, S. Uttam, R. K. Bista, C. Zhao, and Y. Liu, *Opt. Express* **20**(8), 9203–9214 (2012).
- ²²S. A. Alexandrov, S. Uttam, R. K. Bista, K. Staton, and Y. Liu, *Appl. Phys. Lett.* **101**(3), 033702 (2012).
- ²³Y. Liu, S. Uttam, S. Alexandrov, and R. K. Bista, *BMC Biophys.* **7**, 1 (2014).
- ²⁴S. Uttam, S. A. Alexandrov, R. K. Bista, and Y. Liu, *Opt. Express* **21**(6), 7488–7504 (2013).
- ²⁵S. A. Alexandrov, J. McGrath, H. Subhash, F. Boccafosci, C. Giannini, and M. Leahy, *Sci. Rep.* **5**, 13274 (2015).
- ²⁶S. Alexandrov, J. McGrath, C. J. R. Sheppard, F. Boccafosci, C. Giannini, T. Sibillano, H. Subhash, J. Hogan, and M. Leahy, *J. Biophotonics* **11**(7), e201700385 (2018).
- ²⁷S. A. Alexandrov, H. M. Subhash, A. Zam, and M. Leahy, *Nanoscale* **6**(7), 3545–3549 (2014).
- ²⁸S. Alexandrov, H. M. Subhash, and M. Leahy, *Quantum Electron.* **44**(7), 657–653 (2014).
- ²⁹S. Alexandrov, H. M. Subhash, A. Zam, and M. Leahy, U.S. patent 10,012,492 B2 (3 July 2018).
- ³⁰R. Dsouza, J. Won, G. L. Monroy, M. C. Hill, R. G. Porter, M. A. Novak, and S. A. Boppart, *Sci. Rep.* **8**, 8777 (2018).
- ³¹J. McGrath, S. Alexandrov, P. Owens, H. Subhash, and M. Leahy, *J. Biomed. Opt.* **21**(4), 046004 (2016).
- ³²S. Flury, S. Hayoz, A. Peutzfeldt, J. Husler, and A. Lussi, *Dent. Mater.* **28**(5), 521–528 (2012).
- ³³P. H. Tomlins, M. W. Rahman, and R. S. Donnan, *J. Biomed. Opt.* **21**(4), 046001 (2016).
- ³⁴C. J. Kleverlaan and A. J. Feilzer, *Dent. Mater.* **21**(12), 1150–1157 (2005).
- ³⁵R. Dsouza, H. Subhash, K. Neuhaus, R. Kantamneni, P. M. McNamara, J. Hogan, C. Wilson, and M. Leahy, *Laser Surg. Med.* **48**(1), 77–82 (2016).